

# Cold Fronts and Shocks Formed by Gas Streams in Galaxy Clusters

E. Zinger<sup>1\*</sup>, A. Dekel<sup>1</sup>, Y. Birnboim<sup>1,2</sup>, D. Nagai<sup>3</sup>, E. Lau<sup>3</sup> & A. V. Kravtsov<sup>4</sup>

<sup>1</sup>*Center for Astrophysics and Planetary Science, Racah Institute of Physics, The Hebrew University, Jerusalem 91904, Israel*

<sup>2</sup>*Research School of Astronomy and Astrophysics, Australian National University, Canberra, ACT 2611, Australia*

<sup>3</sup>*Department of Physics, Yale University, New Haven, CT 06520, USA*

<sup>4</sup>*Department of Astronomy & Astrophysics, The University of Chicago, Chicago, IL 60637 USA*

Submitted to MNRAS 16 September 2016

## ABSTRACT

Cold Fronts and shocks are hallmarks of the complex intra-cluster medium (ICM) in galaxy clusters. They are thought to occur due to gas motions within the ICM and are often attributed to galaxy mergers within the cluster. Using hydro-cosmological simulations of clusters of galaxies, we show that collisions of inflowing gas streams, seen to penetrate to the very centre of about half the clusters, offer an additional mechanism for the formation of shocks and cold fronts in cluster cores. Unlike episodic merger events, a gas stream inflow persists over a period of several Gyrs and it could generate a particular pattern of multiple cold fronts and shocks.

**Key words:** galaxies: clusters: general – galaxies: clusters: intracluster medium

## 1 INTRODUCTION

X-ray observations of the gaseous Intra-Cluster Medium (ICM) reveal it is rife with features including merging substructures, cavities, shock waves and Cold Fronts (CF) (Markevitch & Vikhlinin 2007).

The Cold Fronts are contact discontinuities of constant or smoothly changing pressure and velocity over a sharp interface between two regions in which one is denser and cooler than its neighbor. A discontinuous drop in temperature across the interface is paired with a jump in density. If no significant non-thermal pressure components are present, the temperature and density contrasts across the interface will be inversely equal.

Shocks on the other hand are characterized by discontinuous jumps in the pressure, density and temperature, all of which increase in value across the shock front. The two phenomena are connected since many processes by which a shock is formed also entail the formation of a contact discontinuity behind it.

CFs are very common in clusters (see Markevitch & Vikhlinin 2007 for a comprehensive review) and have been found in a variety of sizes and shapes (e.g. concentric arcs, filaments, radial or spiral) both in observations (Ghizzardi et al. 2010) and simulations (Bialek et al. 2002; Nagai & Kravtsov 2003; Hallman et al. 2010), and are found in all environments (e.g. disturbed versus quiescent). The accepted measure of a CF strength is the density or temperature con-

trast which is commonly observed to be scattered about a value of  $\simeq 2$  (Owers et al. 2009). In many cases a jump in gas metallicity is also observed, possibly suggesting that enriched low entropy gas stripped from satellite galaxies in the cluster is at play (Markevitch et al. 2000). Signatures of substantial shear flows in CF were detected in relaxed cores (Keshet et al. 2010). Reiss & Keshet (2014) found evidence for strong magnetic fields parallel to the CF, which may contribute to their stability.

Several different mechanisms have been put forward to explain the origin of CFs. They may form as the interface between the low entropy gas left over from merging satellites and the hot diffuse ICM (Markevitch et al. 2000). Other mechanisms invoke shocks, since contact discontinuities are often found behind shocks. Many processes which can induce shocks in the ICM will lead to the formation of CFs: merging substructure (Nagai & Kravtsov 2003; Owers et al. 2011), ‘gas sloshing’ about the centre of the potential well of the cluster due to mergers (Churazov et al. 2003; Ascasibar & Markevitch 2006; ZuHone et al. 2010, 2013) or oscillations of the dark Matter distribution (Tittley & Henriksen 2005). Birnboim et al. (2010) showed that when trailing shocks merge a CF is formed and thus co-centric CFs in the ICM can be the result of shocks which originated at the centre and merged with the virial accretion shock in the past.

In this paper we suggest yet another mechanism for generating shocks and CFs in the ICM, related to the smooth accretion of mass into the cluster. In the past decade, the issue of gas accretion on to galaxies and clusters has been overhauled, with the idealized spherical infall scenario

\* E-mail: elad.zinger@mail.huji.ac.il

(White & Rees 1978) being replaced by accretion that occurs predominately along filamentary streams which flow along the large-scale dark matter cosmic web (Birnbom & Dekel 2003; Kereš et al. 2005; Dekel & Birnbom 2006; Dekel et al. 2009; Kereš et al. 2009).

Two modes of gas accretion are identified in cosmological simulations in galactic haloes at high redshift: hot gas which has been shock-heated by the virial shock and accretes spherically via cooling to the centre and cold gas which accretes through dense filaments which, due to their higher density and shorter cooling times, are impervious to the formation of a shock (Birnbom & Dekel 2003). The cold mode accretion is dominant for low-mass haloes while the hot mode accretion becomes more important for high-mass haloes (Dekel & Birnbom 2006). The new understanding that gas streams are an important feature in the formation of galaxies and clusters, especially in terms of mass accretion into the system, may have far reaching implications on the way cluster-sized systems are formed and maintained.

Dekel & Birnbom (2006) and Dekel et al. (2009) show that the coexistence of the hot and cold modes of accretion reflects the interplay between the shock-heating scale and the dark matter non-linear clustering scale (the Press-Schechter mass),  $M_*$ . In standard cosmologies, the large-scale structure of the dark matter is roughly self-similar. Haloes of mass  $\sim M_*$  are embedded within the filaments and as a result, mass infall will be scattered over a wide solid angle. In the much rarer haloes of  $M \gg M_*$ , and galaxy clusters fall firmly into this category, the accretion will be predominately along filaments which are thin in comparison to the halo size, and significantly denser than their host haloes.

As discussed in Zinger et al. (2016), the filamentary streams which were the predominant form of mass accretion into galaxies at high redshift, are still found in clusters at  $z = 0$  and are still the channel in which most of the mass accretion into the cluster takes places.

For massive filaments, more massive than  $10^{12} M_\odot / \text{Mpc}$ , a shock is expected to form at the edges of filaments. These will likely feed low-redshift clusters with  $M_{\text{halo}} \gtrsim 10^{15} M_\odot$  (Birnbom et al. 2016). As we shall see below, a shock forms even for slightly lower masses, heating the gas to  $\gtrsim 10^6 \text{ K}$  prior to its entry to the cluster virial radius. The gas is further heated as it flows towards the centre and by the time it reaches the inner regions of the cluster, the gas stream is at the virial temperature, no longer cooler than the ambient gas. In half the clusters examined in Zinger et al. (2016) at  $z = 0$ , the inflowing streams were seen to penetrate into the very centre of the cluster. All of these clusters were classified as dynamically ‘unrelaxed’, whereas none of the ‘relaxed’ clusters was found to host deeply penetrating streams.

The purpose of this paper is to demonstrate that shocks and CFs can be generated by the inflowing gas streams in clusters and to this end we have chosen to focus with some detail on three cluster outputs, where this phenomenon is convincingly exhibited.

The paper is organized as follows. In §2, we treat the case of gas stream collision and CF formation via a simple analytic model. In §3, we describe the simulations used for the analysis and in §4 we present three representative examples of gas streams colliding in simulated clusters and

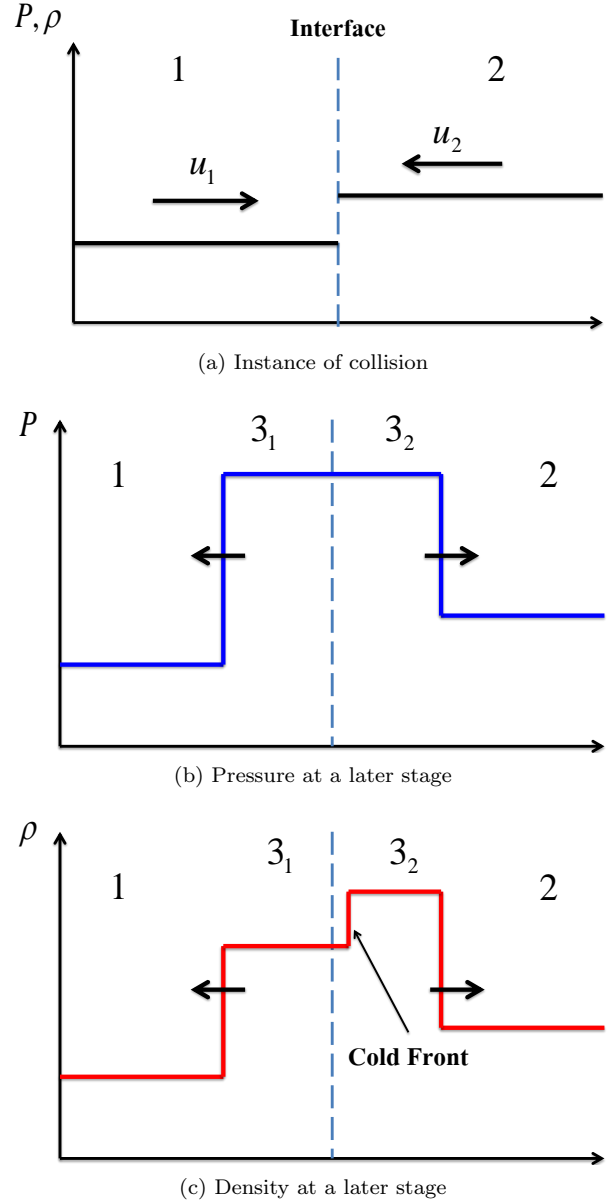


**Figure 1.** Schematic representation of the collision between two homogeneous media. In the instance of collision (a), two media of constant pressure and density are colliding. At a later time, two shocks have formed and are propagating in opposite directions. Between the two shocks a third post-shock state of constant pressure and velocity has formed (b). The density in the post shock (c) region has one of two values (set by the jump conditions for each shock wave) bridged by a contact discontinuity which forms at the Lagrangian location of the initial collision site and moves at the post-shock velocity.

forming shocks and CFs. In §5 we examine the potential for observationally detecting the CFs and shocks in our examples and in §6 we summarize and discuss our findings.

## 2 COLD FRONTS AND SHOCKS GENERATED BY COLLIDING STREAMS

In this section we present a simple analytic toy-model demonstrating that how a collision between an inflowing

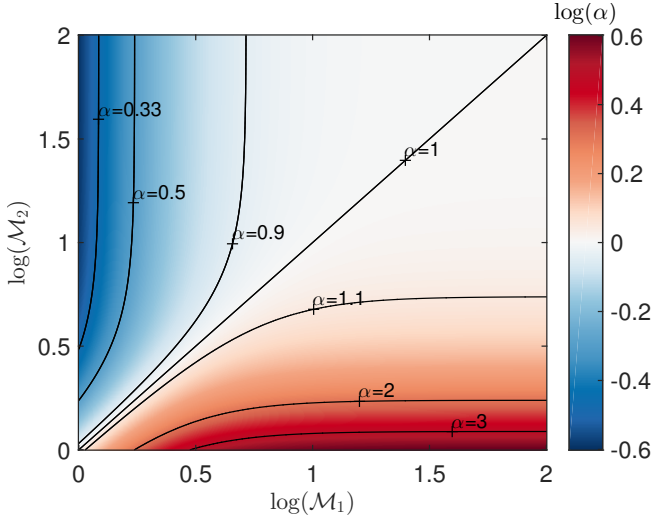


**Figure 2.** The value of the ratio of the post-shock density contrast to the initial density contrast  $\alpha = q/q_0$  in an idealized stream collision scenario for a range of Mach numbers for the two shocks, for an ideal mono-atomic gas with  $\gamma = 5/3$ . Contours mark significant values of  $\alpha$ . We find that  $\alpha \approx 1$  (white regions) for a large range of values, especially in the strong shock regime.

stream with the ambient gas or with another stream can lead to the formation of shocks and CFs, and what is the resultant spatial configuration of the shocks and CFs. Readers interested only in the simulation results may safely skip this section.

In clusters possessing deeply penetrating streams, the inflowing streams can collide with each other or with the ambient gas, leading to the formation of shocks and CFs. At the moment of collision, we find two regions whose relative velocity is converging.

As an illustrative case, consider a 1-Dimensional problem of two compressible gaseous regions (ideal gases with a similar equation of state), marked by 1 and 2, each of constant density  $\rho_i$ , pressure  $P_i$  and velocity  $U_i$ , with subscript  $i$  for regions 1 and 2, a configuration commonly known as the Riemann Problem (Zel'Dovich & Raizer 2002). We assume that the regions are colliding,  $\Delta U = U_2 - U_1 < 0$ , so there always exists a frame of reference in which the velocities are of opposite sign (Fig. 1a). Two of the four cases of the Riemann problem apply for this velocity condition: either two shocks form, propagating in opposite directions (Figs. 1b and 1c, or a shock and a rarefaction wave form, also propagating in opposite directions (Zel'Dovich & Raizer 2002). As we shall see in §4, the typical high inflow velocities of the streams ( $\sim 1000 \text{ km s}^{-1}$ ) and the details of the collisions make the double shock configuration the preferred scenario in the central regions of clusters. In the following paragraphs we solve the double-shock scenario in detail.

We can solve the system by treating each of the shocks separately and utilizing the Rankine-Hugoniot shock jump conditions (Landau & Lifshitz 1959) to find the state of the post shock gas behind each shock, which we mark as zone 3<sub>1</sub> and 3<sub>2</sub>.

The jump conditions for the shocks propagating into

zones  $i = 1, 2$  are

$$P_{3,i} = P_i \frac{2\gamma\mathcal{M}_i^2 - (\gamma - 1)}{\gamma + 1} \quad (1)$$

$$U_{3,i} = U_i + \frac{P_{3,i} - P_i}{\rho_i(V_i - U_i)} \quad (2)$$

$$\rho_{3,i} = \rho_i \frac{U_i - V_i}{U_{3,i} - V_i}, \quad (3)$$

where  $V_{1,2}$  are the velocities of the two shocks, the Mach numbers are defined as the ratio of the velocity to the sound speed for each region  $\mathcal{M}_i \equiv U_i/c_i$  and the speed of sound in the pre-shock region given by

$$c_i = \sqrt{\gamma \frac{P_i}{\rho_i}}. \quad (4)$$

The shock velocities for the two shocks are

$$V_1 = U_1 - \mathcal{M}_1 c_1 \quad (5)$$

$$V_2 = U_2 + \mathcal{M}_2 c_2, \quad (6)$$

with the difference in sign for the second term in eqs. (5) and (6) due to the shocks propagating in opposite directions.

Since there is no inherent time or length scale in this problem, the solution for it will be self-similar, which entails that the post-shock gas must be in pressure equilibrium, and of uniform velocity (Zel'Dovich & Raizer 2002)

$$P_3 = P_{3,1} = P_{3,2} \quad (7)$$

$$U_3 = U_{3,1} = U_{3,2}. \quad (8)$$

Under these constraints, the jump conditions eqs. (1) to (3), can be restated resulting in the following implicit equations which can be solved numerically to obtain the Mach numbers for the shocks

$$\frac{2\gamma\mathcal{M}_2^2 - (\gamma - 1)}{2\gamma\mathcal{M}_1^2 - (\gamma - 1)} = \frac{P_1}{P_2} \quad (9)$$

$$\frac{\gamma - 1}{2} (U_1 - U_2) = -\frac{\gamma - 1}{2} \Delta U = c_1 \left( \mathcal{M}_1 - \frac{1}{\mathcal{M}_1} \right) + c_2 \left( \mathcal{M}_2 - \frac{1}{\mathcal{M}_2} \right), \quad (10)$$

where we recall that we have set  $\Delta U < 0$ .

Once the Mach numbers are known, the post shock velocity, eq. (8) can be solved for

$$U_3 = \frac{U_1 + U_2}{2} + \frac{1}{\gamma - 1} \left[ c_1 \left( \mathcal{M}_1 - \frac{1}{\mathcal{M}_1} \right) - c_2 \left( \mathcal{M}_2 - \frac{1}{\mathcal{M}_2} \right) \right]. \quad (11)$$

In addition, we define the density contrast across the contact discontinuity as the ratio between the two densities in the post-shock regions as

$$q \equiv \frac{\rho_{3,1}}{\rho_{3,2}} = \frac{\rho_1 \gamma - 1 + 2\mathcal{M}_2^{-2}}{\rho_2 \gamma - 1 + 2\mathcal{M}_1^{-2}}. \quad (12)$$

The density contrast is a natural measure for the prominence of the contact discontinuity.

We find that a contact discontinuity ( $q \neq 1$ ), i.e. a CF, should occur whenever a stream collides, either with other streams or with the ambient gas in the cluster. The CF will form at the Lagrangian location of the initial interface (Fig. 1c) and travel at the post-shock velocity  $U_3$ . Only in

the very unlikely case of  $\rho_1 = \rho_2$  and  $P_1 = P_2$  a CF will not form.

We now explore the relation of the density contrast of the CF,  $q$  to the initial density contrast between the streams  $\rho_1/\rho_2$ . We re-write eq. (12) as

$$q = q_0 \alpha(\mathcal{M}_1, \mathcal{M}_2; \gamma), \quad (13)$$

with  $q_0 = \rho_1/\rho_2$  and

$$\alpha(\mathcal{M}_1, \mathcal{M}_2; \gamma) = \frac{\gamma - 1 + 2\mathcal{M}_2^{-2}}{\gamma - 1 + 2\mathcal{M}_1^{-2}}. \quad (14)$$

It is important to note that  $\mathcal{M}_1$  and  $\mathcal{M}_2$  are *not* independent of  $q_0$  and that this formulation is useful for deducing the initial density contrast by observing the system at a developed state.

In Fig. 2 we plot the value of  $\alpha$  for a range of Mach numbers for the two shocks. Naturally, the high density region is always on the side of the stronger shock. For a large range of values, especially in the strong shock regime ( $\mathcal{M} > 10$ ),  $\alpha \approx 1$ . The maximal and minimal values of  $\alpha$  are obtained when one shock is very strong and the other very weak

$$\frac{\gamma + 1}{\gamma - 1} < \alpha < \frac{\gamma - 1}{\gamma + 1}, \quad (15)$$

which for  $\gamma = 5/3$  is  $1/4 < \alpha < 4$ . We note that shocks found in the central regions of the ICM are typically weak shocks.

The solution presented above is valid for most reasonable collision situations, however it is possible to construct initial conditions where this solution is not valid. In the limit of  $\Delta U \rightarrow 0$ , eq. (10) can only be satisfied for  $\mathcal{M}_1 \approx \mathcal{M}_2 \approx 1$ , a condition that cannot be satisfied simultaneously with eq. (9) for all values of  $P_1/P_2$ . The physical interpretation of this is that, assuming  $P_2 > P_1$ , for a given value of  $P_1/P_2$ , there exists a critical velocity difference  $\Delta U_C$ , such that for collisions with lower velocity difference (in absolute value) the resulting post-shock pressure is  $P_3 < P_2$ .

Under these conditions, the second case of the Riemann problem becomes relevant, namely a single shock wave propagating into zone 1 (since we assumed  $P_1 < P_2$ ) which raises the pressure to  $P_3$  in the post-shock gas, and a rarefaction wave propagating into zone 2 which *lowers* the pressure to  $P_3$ , as in the solution to the ‘shock tube problem’ (see e.g. Zel’Dovich & Raizer 2002, Chap. 4). The medium between the shock wave and rarefaction wave is also in pressure equilibrium and contains a contact discontinuity, but its density contrast will naturally *not* be given by eq. (12). As we shall see, this scenario not expected in collision sites of the streams in the central regions of the clusters, due to the very high velocities associated with the streams.

The 1D scenario explored in this section is very idealized and does not address many of the properties and processes found in the ICM such as turbulent motions, radiative cooling, gravity etc., but as we shall see, it still captures the essential aspects of the process leading to the formation of CFs in the ICM.

### 3 SIMULATIONS

The simulations were carried out with the Adaptive Refinement Tree (ART)  $N$ -body +gas-dynamics code (Kravtsov

Cluster	Redshift $z$	$M_{\text{vir}}$ [ $10^{14} M_{\odot}$ ]	$R_{\text{vir}}$ [Mpc]	$T_{\text{vir}}$ [ $10^7$ K]	$V_{\text{vir}}$ [ $\text{km s}^{-1}$ ]
CL6	0	3.3	1.80	2.9	894
CL6	0.6	2.4	1.15	3.2	946
CL107	0	6.6	2.26	4.5	1125

**Table 1.** Properties of the dynamically active clusters CL6 at  $z = 0$  and  $z = 0.6$  and CL107 at  $z = 0$ . Virial quantities were calculated for an over-density of  $\Delta_{\text{vir}} = 337$ .

1999), an Eulerian code that uses adaptive refinement in space and time, and (non-adaptive) refinement in mass (Klypin et al. 2001) to reach the high dynamic range required to resolve cores of haloes formed in self-consistent cosmological simulations.

The systems were extracted from cosmological simulations in a flat  $\Lambda$ CDM model:  $\Omega_m = 1 - \Omega_{\Lambda} = 0.3$ ,  $\Omega_b = 0.04286$ ,  $h = 0.7$ , and  $\sigma_8 = 0.9$ , where the Hubble constant is defined as  $100h \text{ km s}^{-1} \text{ Mpc}^{-1}$ , and  $\sigma_8$  is the power spectrum normalization on an  $8h^{-1} \text{ Mpc}$  scale. The computational boxes of the large-scale cosmological simulations were either  $80h^{-1} \text{ Mpc}$  (CL6, see §4.1) or  $120h^{-1} \text{ Mpc}$  (CL107, see §4.2), and the simulation grid was adaptively refined to achieve a peak spatial resolution of  $\sim 7h^{-1}$  and  $5h^{-1} \text{ kpc}$  respectively. These simulations are described in detail in Kravtsov et al. (2006), Nagai et al. (2007b) and Nagai et al. (2007a). Adaptive mesh refinement techniques, such as the one employed in the simulation, are particularly suited to capture discontinuous features such as shocks and contact discontinuities which make it especially suitable for our purposes.

The simulation suite analysed in this study is comprised of 16 cluster-sized systems at  $z = 0$  spanning a mass range of  $8.6 \times 10^{13} - 2.2 \times 10^{15} M_{\odot}$ , and their most massive progenitors at  $z = 0.6$ . In this paper we have chosen to focus on two clusters, CL6, in which a clear and compelling example of our proposed mechanism is realized (§4.1), and CL107 in which the compound effect of stream collision and a satellite give rise to shocks and CFs (§4.2).

The gas in the simulations is treated as a mono-atomic ideal gas, and is thus well described by an equation of state

$$P = (\gamma - 1)\rho e, \quad (16)$$

where  $P$ ,  $\rho$  and  $e$  are the pressure, density and specific internal energy respectively and  $\gamma$  is the adiabatic index ( $\gamma = 5/3$  for a mono-atomic gas).

Besides the basic dynamical processes of collision-less matter (dark matter and stars) and gas-dynamics, several physical processes critical for galaxy formation are incorporated: star formation, metal enrichment and feedback due to Type II and Type Ia supernovae, and self-consistent advection of metals. The cooling and heating rates take into account Compton heating and cooling of plasma, heating by the UV background (Haardt & Madau 1996), and atomic and molecular cooling, which is tabulated for the temperature range  $10^2$  to  $10^9 \text{ K}$ , a grid of metallicities, and UV intensities using the CLOUDY code (version 96b4; Ferland et al. 1998). The CLOUDY cooling and heating rates take into account metallicity of the gas, which is calculated self-consistently in the simulation, so that the local cooling rates depend on the local metallicity of the gas. The star formation



recipe incorporated in these simulations is observationally motivated (e.g. Kennicutt 1998) and the code also accounts for the stellar feedback on the surrounding gas, including injection of energy and heavy elements (metals) via stellar winds, supernovæ, and secular mass loss.

The simulations do *not* include AGN feedback mechanisms, and while this may lead to unrealistic conditions in the core of the cluster, it allows us to isolate the role of the gas streams in determining the conditions in the inner regions of the ICM from that of the AGN.

The virial quantities of the mass, radius, temperature and velocity ( $M_{\text{vir}}$ ,  $R_{\text{vir}}$ ,  $T_{\text{vir}}$ , &  $V_{\text{vir}}$ ) of the clusters are defined for an over-density  $\Delta_{\text{vir}} = 337$  at  $z = 0$  and  $\Delta_{\text{vir}} = 224$  at  $z = 0.6$  (Bryan & Norman 1998) above the mean density of the universe. The properties of the dynamically active ‘unrelaxed’ clusters at  $z = 0$  and  $z = 0.6$  are summarized in Table 1.

The simulations of the clusters were classified visually as ‘relaxed’ or ‘unrelaxed’. The classification was carried out to emulate as close as possible the methods employed by observational studies. The classification is described in detail in Nagai et al. (2007a,b), and is based on mock *Chandra* X-ray images of the clusters. Based on the mock observations, clusters were classified as relaxed if they possessed regular X-ray morphology and a single luminosity peak, with minimal deviation of the isophotes from elliptical symmetry. In contrast, unrelaxed clusters are those with secondary luminosity peaks, filamentary X-ray structures, or significant shifts in the centres of the isophotes. A cluster was deemed unrelaxed if it appeared so in at least one of the 3 orthogonal Cartesian projections. In this work, we focus on analysing the dynamically active clusters that exhibit prominent features of shocks and CFs.

The gas velocities are shown with respect to an inertial frame defined by a centre-of-mass velocity of the cluster. For each cluster in the suite, a centre-of-mass velocity profile was calculated for the 3 velocity components and a radius was selected where the profiles were seen to level off, typically at  $\sim 1 - 2R_{\text{vir}}$ , and remain nearly constant beyond that. The gas velocities are then measured with respect to the centre-of-mass velocity as calculated for the gas within that radial limit. As a result, the centre-of-mass velocity is largely insensitive to the choice of the radial limit.

#### 4 COLLIDING STREAMS IN SIMULATED CLUSTERS

In this section we present a representative example of two simulated clusters possessing deeply penetrating streams in which the collision between inflowing streams can be seen to create shocks and CFs in the ICM.

As we have seen, the CF interface is in pressure equilibrium. Since for an ideal gas equation of state  $P \propto \rho T$ , this entails that the temperature and density contrasts are inversely proportional to each other:

$$P_1 = P_2 \rightarrow \rho_1 T_1 = \rho_2 T_2 \rightarrow \frac{T_1}{T_2} = \left( \frac{\rho_1}{\rho_2} \right)^{-1}, \quad (17)$$

where the subscripts 1 and 2 denote the conditions on either side of the interface. We use the proxy for entropy  $S \propto T\rho^{-2/3}$  and find that it is an excellent indicator of CFs in

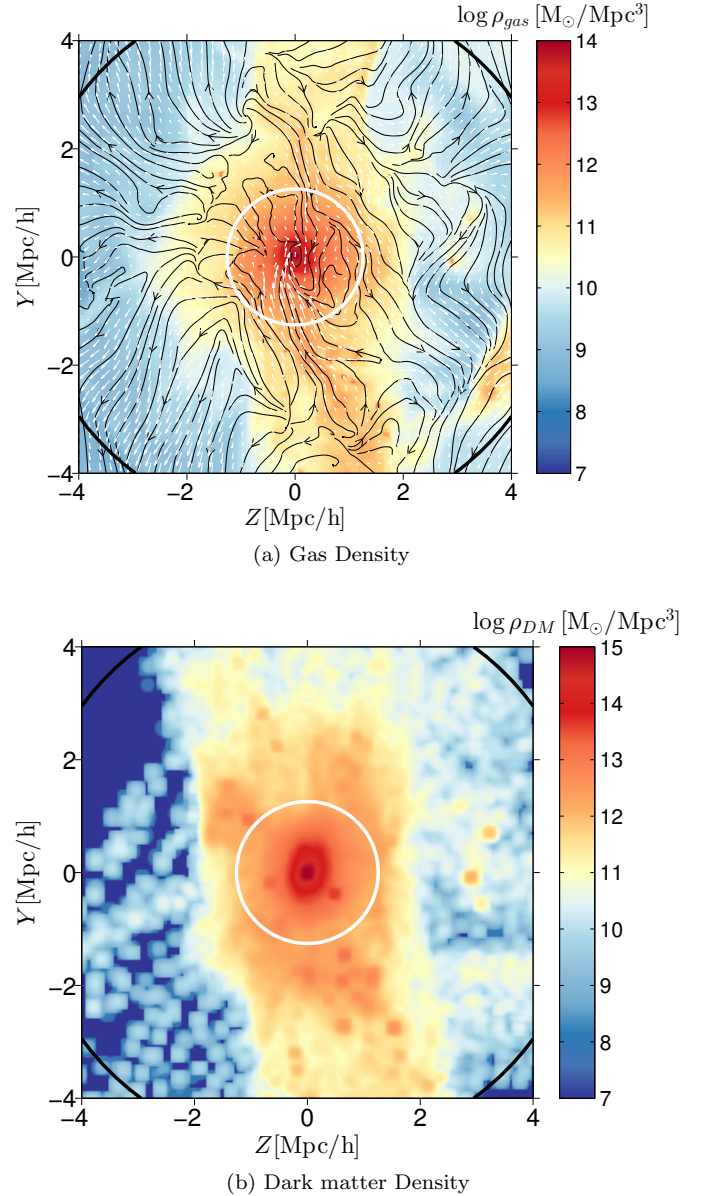


**Figure 3.** Gas and dark matter density of the cluster CL6 at  $z = 0$ , (a) & (b), respectively. The white circles denote the virial radius of the cluster and the black circles demark the approximation location of the virial accretion shock (in this projection). The velocity field is shown as arrows (white) and streamlines (black) in (a). The values shown are averaged over a slice of  $500h^{-1}$  kpc.

simulations

$$\frac{S_1}{S_2} = \frac{T_1}{T_2} \left( \frac{\rho_1}{\rho_2} \right)^{-2/3} = \left( \frac{T_1}{T_2} \right)^{3/5} = \left( \frac{\rho_1}{\rho_2} \right)^{-5/3} = q^{-5/3}. \quad (18)$$

##### 4.1 Colliding Streams in CL6

The cluster CL6 is a  $M_{\text{vir}} = 3.3 \times 10^{14} M_{\odot}$  cluster with a virial radius of  $R_{\text{vir}} = 1.8 \text{ Mpc}$  at  $z = 0$ . Fig. 3 shows the gas and dark matter density of the cluster on a scale of several  $R_{\text{vir}}$ . The cluster is situated along a large scale dark matter filament, whose diameter is  $\sim R_{\text{vir}}$  (Dekel & Birnboim 2006). The accretion shock of the ICM extends to  $\sim 4R_{\text{vir}}$  (Lau et al. 2015, Zinger et al. in preparation). The gas accretion

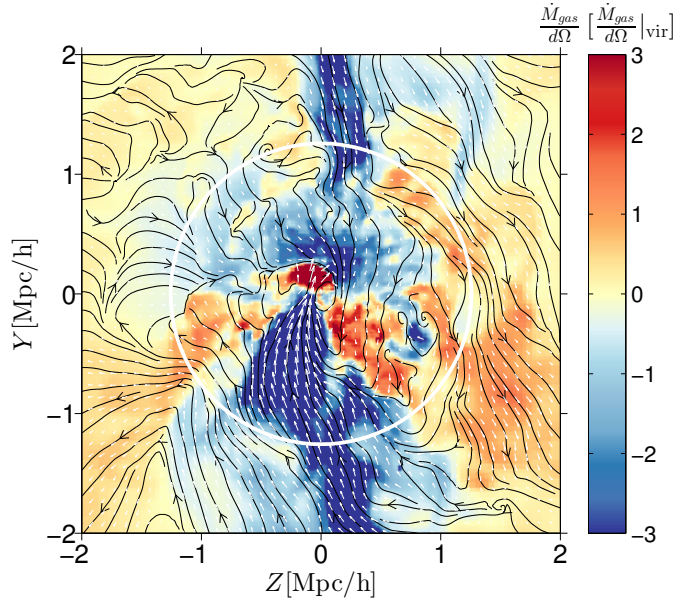


**Figure 4.** The gas mass accretion rate into the simulated cluster CL6 at  $z = 0$ . The virial radius is shown as a white circle. The velocity field is shown as arrows (white) and streamlines (black). The values shown are averaged over a slice of  $100h^{-1}$  kpc. A gas stream is flowing from the bottom upwards, penetrating into the centre and colliding with the ambient gas. A second stream flowing from the top stops just inside the virial radius.

can be seen to occur predominantly through streams which lie along the centre of the dark matter filament.

In Fig. 4 we show the gas mass accretion rate, defined as

$$\dot{M}(r) = \int_{\Omega} \rho [(\vec{v} - \vec{v}_{cm}) \cdot \hat{r}] r^2 d\Omega, \quad (19)$$

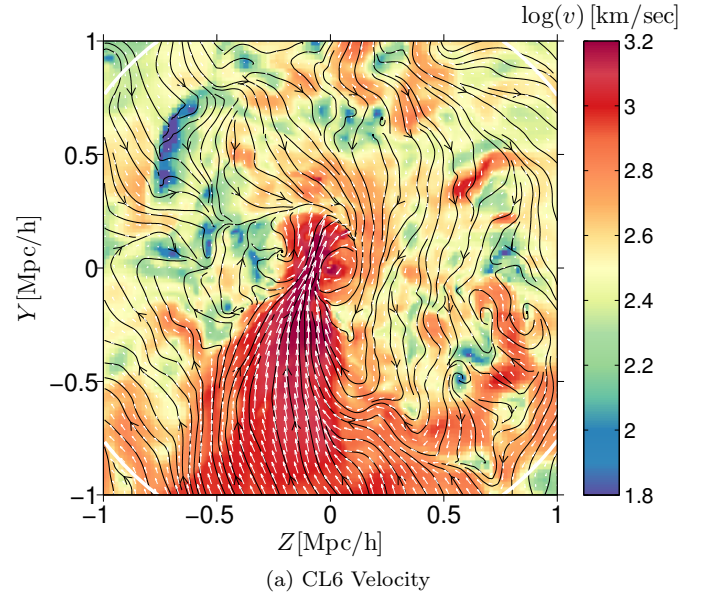
for the cluster. A prominent stream enters from the bottom and flows to the centre, where it collides with the ambient gas which is also flowing inwards. The stream from the bottom actually overshoots the centre (and thus the radial mass accretion rate changes sign abruptly) before colliding with the inflowing gas coming from the top. Another stream can be identified flowing from the top and dissipating just inside the virial radius.

In Fig. 5 we show the local velocity of the gas and its corresponding Mach number  $\mathcal{M} = v/c_s$ , where the typical sound speed is defined for a shell of given radius as

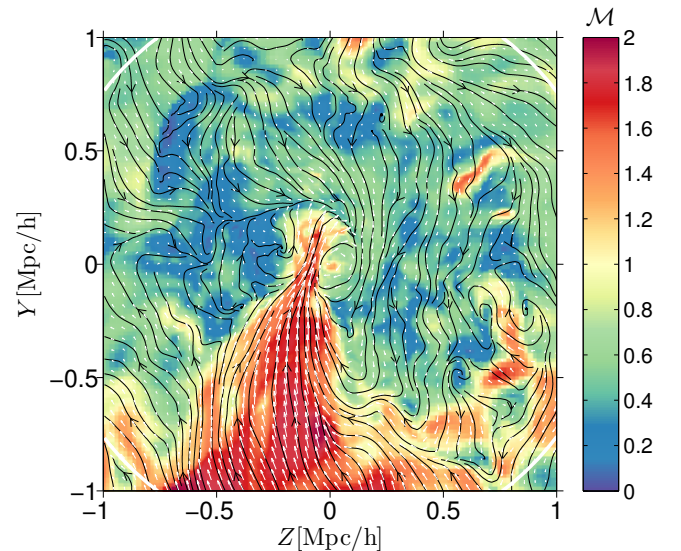
$$c_s(r) = \sqrt{\frac{\partial P}{\partial \rho}}_S = \sqrt{\gamma \frac{k_B \bar{T}}{\mu m_p}}. \quad (20)$$

The second expression derives from the ideal gas equation of state used to describe the gas.  $k_B$  is the Boltzmann constant,  $\mu m_p \simeq 0.59m_p$  is the average particle mass ( $m_p$  is the proton mass) and  $\bar{T}$  is the mass-weighted mean temperature of a spherical shell of radius  $r$ .

The typical velocities are of order  $500 \text{ km s}^{-1}$  for the gas coming from the top and  $1000 \text{ km s}^{-1}$  for the bottom stream, which is moving supersonically with respect to its surrounding. The velocity difference in the collision is of order  $\sim 1500 \text{ km s}^{-1}$ . The Mach numbers of the collisions are thus  $1.5 - 2$ .



(a) CL6 Velocity



(b) CL6 Mach Number

**Figure 5.** The magnitude of gas velocity in the simulated cluster CL6 at  $z = 0$  is shown in (a) and the corresponding Mach number  $\mathcal{M} = v/c_s$  for the flow shown in (b). The virial radius is shown as a white circle (see at the corners of the plots). The velocity field is shown as arrows (white) and streamlines (black). The values shown are averaged over a slice along the  $X$  plane of  $50h^{-1}$  kpc. A high velocity ( $\gtrsim 1000 \text{ km s}^{-1}$ ) supersonic stream is flowing upwards, overshooting the centre and colliding with the ambient gas which is flowing inwards.

In Fig. 6 we examine in detail the area in which the stream collides with the ambient gas, by showing the various properties of the gas. A shock front propagating upwards is clearly visible in the interface between the two streams (e.g. Fig. 6a) marked by a red arrow. It appears as a sharp discontinuity in the temperature, pressure and density maps (Figs. 6d to 6f) as well as in the velocity field, but only barely distinguishable in the entropy map Fig. 6c.

Just above this shock, another less distinct shock may be identified, especially in the pressure and temperature



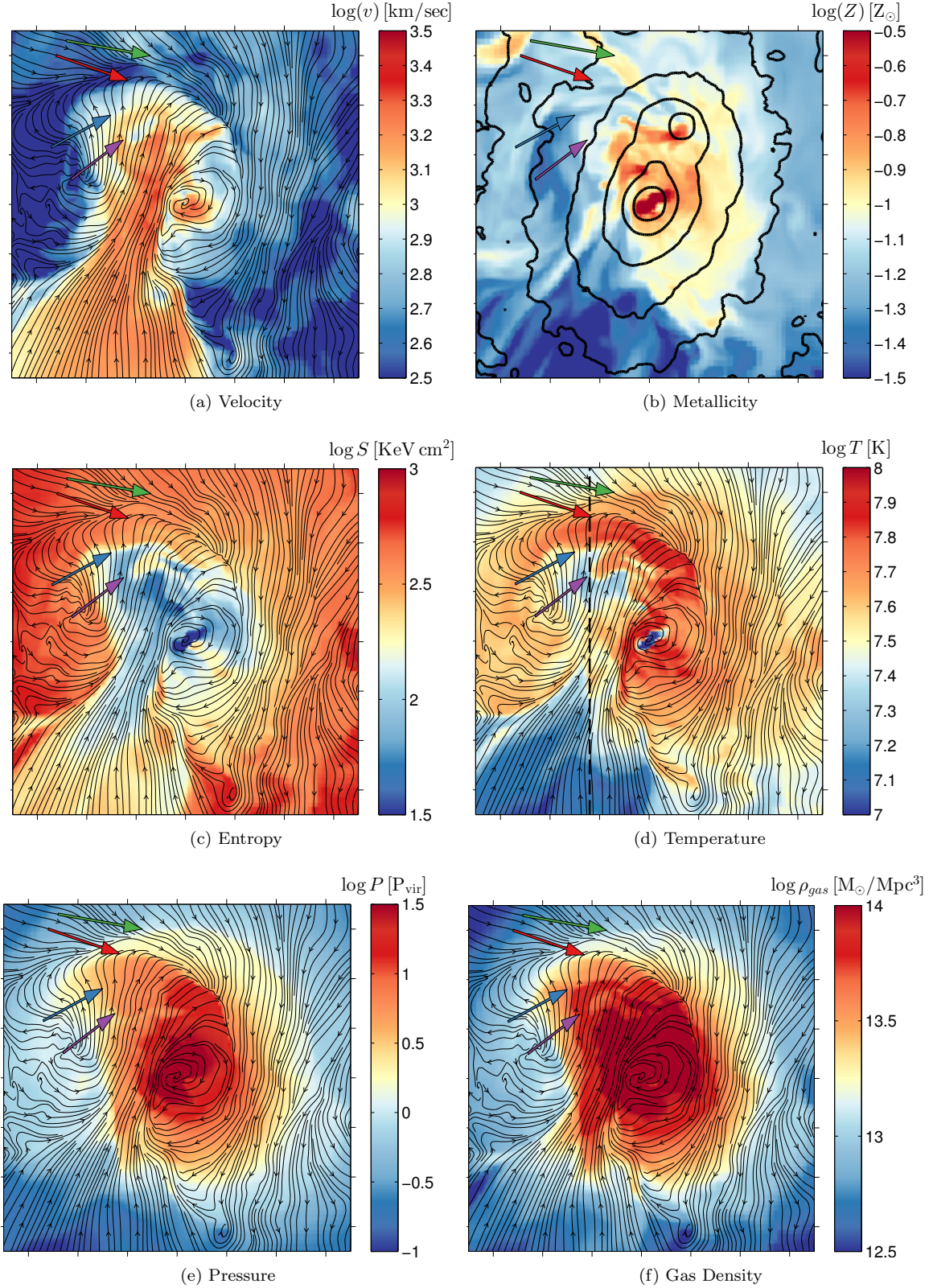


**Figure 6.** The collision zone in CL6 at  $z=0$  is shown in detail in a box of side  $0.7h^{-1}$  Mpc centred on the cluster centre. The velocity (a), metallicity (b), entropy (c), temperature (d), pressure (e) and gas density (f) are all averaged over a slice of  $25h^{-1}$  kpc. Dark matter density contours (black) are shown in (b) (averaged over a slice of width  $50h^{-1}$  kpc). Streamlines represent the velocity field. Areas of interest are marked by colored arrows as follows: the red arrow marks the prominent shock propagating away from the collision site and the green arrow marks another shock, which formed earlier. The blue arrow marks a CF and the purple arrow marks the location of another weaker shock propagating downwards (see Fig. 7). The dashed vertical line in (d) marks the cross-section used to construct the profiles of the gas properties in Fig. 7.

maps (Figs. 6d and 6e). A green arrow marks its position. Since this shock is also propagating upwards, it stands to reason that this shock was formed earlier, perhaps due to a change in the penetration or direction of the gas flow.

Just below the shock front, a prominent CF can be identified, when looking from the shock front downwards, as a drop in entropy and temperature and a rise in gas density (marked by a blue arrow). As expected, the pressure remains constant across the CF. Another feature we suspect of being a shock is barely discernible in these maps, but can be identified when following the profiles of the gas properties as done in Fig. 7. Its position is marked by a purple arrow.

In Fig. 6b the gas metallicity is shown as a color map, overlaid with the dark matter density distribution, in black contours. Just above the central density peak of the cluster a smaller density peak can be identified. This is a sub-halo in the cluster which hosts a satellite galaxy. A tail of high metallicity gas, stripped by ram-pressure and tidal forces, can be seen trailing the satellite.

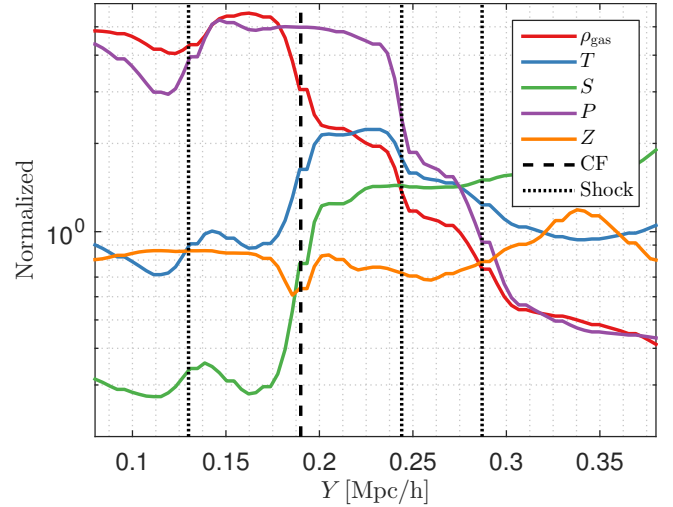
The metallicity in the rest of the gas stream is much lower than the gas in the satellite and central galaxy, leading us to conclude that most of the gas in the stream is *not* gas removed from the satellite. In light of this, and since the satellites are not adjacent to them, we conclude that the shocks and CFs are not the result of the motion of the satellite.

We study the shock fronts and CFs in detail by following the gas properties along a vertical line in the  $Y$  direction of the cluster at a position of  $Z = -0.12h^{-1}$  Mpc (see Fig. 6d). The line chosen is nearly perpendicular to the shock front and CF and will thus allow us to probe the jumps in values of the gas properties. At each point along the line we average<sup>1</sup> the gas properties in the plane perpendicular to the line ( $X - Z$  plane) on a scale of 40 kpc.

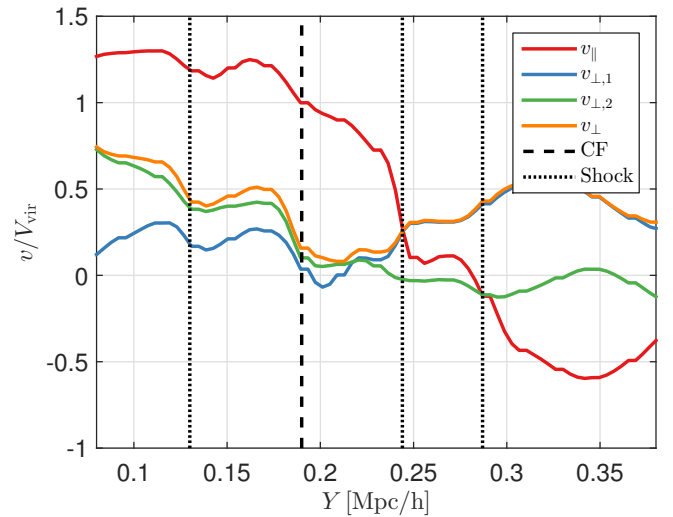
In Fig. 7a we show the profiles in the vicinity of the shock and CF for the gas density, temperature, entropy pressure and metallicity while the velocity component parallel ( $v_y$ ) and perpendicular ( $v_x$  and  $v_y$ ) to the reference line are shown in Fig. 7b. The locations of shocks and CFs are also marked. The profiles are in units of virial parameters (or combinations of them): density is in units of  $\rho_{\text{vir}} \equiv \Delta_{\text{vir}} \rho_{\text{mean}}$ , temperature in units of  $T_{\text{vir}}$ , entropy in units of  $T_{\text{vir}}/\rho_{\text{vir}}^{3/2}$  and pressure in units  $\rho_{\text{vir}} T_{\text{vir}}$ . Metallicity is in units of  $0.1Z_{\odot}$  and the velocity components are in units of  $V_{\text{vir}}$ .

It is common to separate the velocity at a discontinuity into two components: one parallel and one perpendicular *to the discontinuity*. In our treatment, the orientation of the discontinuity is not defined, and instead we choose a reference line which is roughly perpendicular to the discontinuity (see Fig. 6d). We find it more precise to define the velocity components with respect to the reference line, so the velocity component parallel to the line is a good approximation to the velocity component which is perpendicular to the discontinuities, and vice-versa.

A closer examination of the profiles reveals that there are indeed two shock fronts at the collision site, as evident by the jumps in pressure, density, temperature and the velocity component perpendicular to the shock front. Both



(a) Thermodynamic Properties



(b) Velocity Components

**Figure 7.** Profiles of the gas properties in CL6 at  $z = 0$  along a line in the  $Y$  direction (and  $X = 0$ ), perpendicular to the shock and CF, at  $Z = -0.12h^{-1}$  Mpc (see Fig. 6d). Gas density (red), temperature (blue), entropy (green) pressure (purple) and metallicity (orange) are shown in (a). The parameters are all in units of the virial parameters except for metallicity, which is units of  $0.1Z_{\odot}$ . The velocity components parallel (red) and perpendicular (orange) to the line are shown in (b).  $v_{\perp}$  is decomposed into two components  $v_{\perp,1} = v_z$  (blue) in the plane of Fig. 6 and  $v_{\perp,2} = v_x$  (green) perpendicular to it. Locations of shock fronts and CFs are also marked by black dotted and black dashed lines, respectively. The double shock configuration, with CF between them, as described in §2 appears to have been realized in the simulated cluster.

propagating towards the right in Fig. 7, which is upwards in Fig. 6. The topmost shock is found at  $Y \sim 0.29h^{-1}$  Mpc and the second, more prominent shock at  $Y \sim 0.24h^{-1}$  Mpc. The Mach number for the shocks can be deduced from the jump in pressure (eq. 1) and the shock velocity can then be calculated from eq. (5), finding  $u_{s,1} \simeq 1580 \text{ km s}^{-1}$  ( $\mathcal{M}_1 \simeq 1.5$ ) for the lower shock (indicated by a red arrow in Fig. 6) and  $u_{s,2} \simeq 840 \text{ km s}^{-1}$  ( $\mathcal{M}_2 \simeq 1.5$ ) for the upper shock (indicated by a green arrow in Fig. 6).

<sup>1</sup> Temperature and entropy averages are mass weighted.



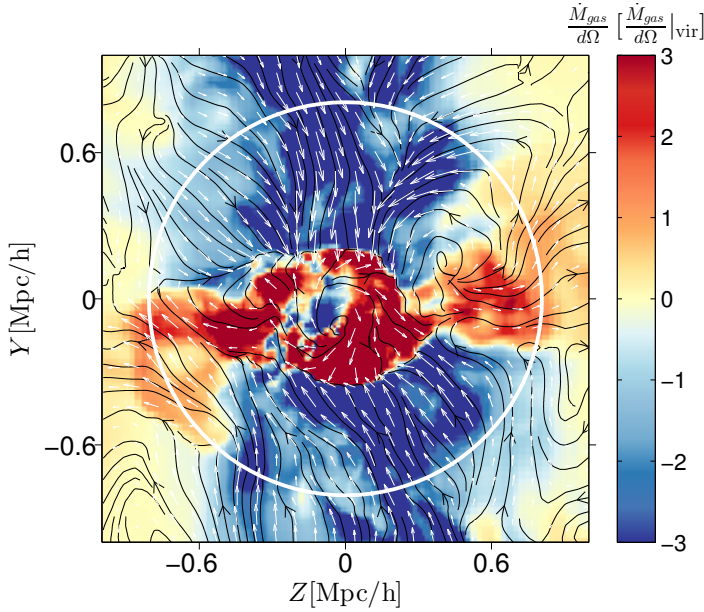


**Figure 8.** Mass inflow rate of CL6 at  $z = 0.6$ .  $R_{vir}$  is marked by a white circle, with the velocity field shown as arrows (white) and streamlines (black). Two streams flow into the cluster from the top and bottom and reach the centre where they are stopped by shock waves. Values are averaged over a slice of  $125h^{-1}$  kpc.

We thus have a situation in which the weaker shock might be overtaken by the stronger one in  $\sim 350$  Myr, which might lead to the formation of an additional CF when these two shocks merge (Birnbom et al. 2010).

Below the shock front, at a position of  $Y = 0.19h^{-1}$  Mpc we find the distinct CF with a sharp rise in temperature, with a contrast of  $q \simeq 2.4$  and an equal (to within a few per cent) drop in density (along the positive  $Y$  direction), which ensures pressure equilibrium. The metallicity across the CF is roughly constant, making it unlikely that the CF was formed due to gas stripping from a satellite. The velocity component perpendicular to the CF is continuous (unlike a shock) while a jump is found in the tangential components (Fig. 7b).

At a position of  $Y = 0.13h^{-1}$  Mpc we find another feature we suspect of being a shock, though the gradient along the line is not as sharp as the other shock features, most likely due to inclination of the shock front with respect to the reference line (Fig. 6e). If this is indeed a shock, it is propagating downwards and we find that the idealized scenario presented in §2 has been realized in the simulation, with two shocks moving in opposite directions<sup>2</sup>, with a CF in between the two. The Mach number and velocity of this shock are  $\mathcal{M}_3 \simeq 1.3$  and  $u_{s,3} \simeq -280 \text{ km s}^{-1}$ , respectively.

In Fig. 8 we show the mass inflow rate of the cluster CL6 at an earlier epoch of  $z = 0.6$ , with the temperature and density in the centre of the cluster at that time shown in Fig. 9. The inflowing streams existed back then in a similar configuration, with some notable differences. At  $z = 0.6$  we find two streams, one flowing from the top (which at

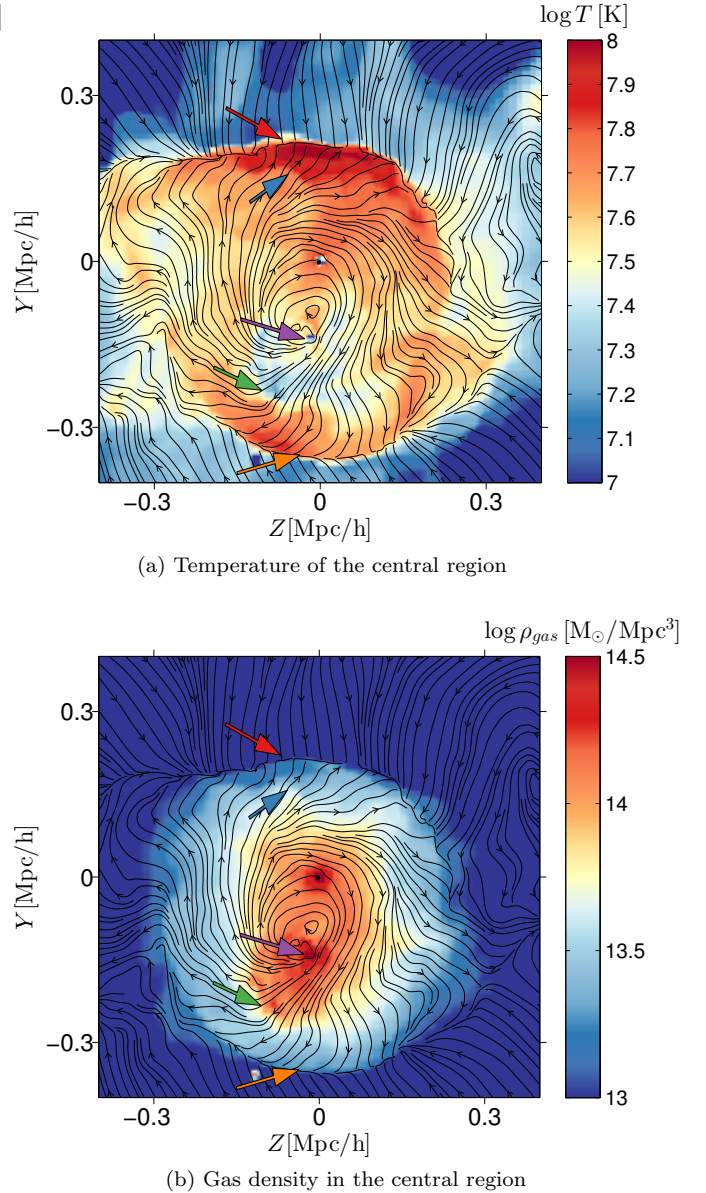


**Figure 9.** The temperature (a) and density (b) of the gas in the central region of CL6 at  $z = 0.6$ . We identify two shocks (red & orange arrows) propagating into the streams as well as the CFs (blue & green arrows). A large satellite is discernible just below the central galaxy marked by a purple arrow. The CF marked by the green arrow is very pronounced due to high metallicity gas stripped by the satellite. All maps are averaged over a slice of  $125h^{-1}$  kpc.

$z = 0$  was stopped at the virial radius) and another from the bottom towards the centre where two large shocks can be seen propagating back into the streams, marked by red and orange arrows in Fig. 9a, in a configuration similar to the ideal 1D model discussed in §2. CFs can also be identified in the pictures (as indicated by blue and green arrows).

A large satellite can be identified just below the central galaxy, and the cooler gas found just above the lower CF (marked by the green arrow) contains high-metallicity gas stripped from the satellite. The formation of the lower CF

<sup>2</sup> The velocities of the shocks are both positive to an outside observer, but the shocks are receding from each other.

is therefore due at least in part to the gas removed from the satellite galaxy.

This is hardly surprising since in the period of 5.7 Gyr between the two epochs, much can happen in a dynamically unrelaxed cluster such as this one. In a detailed analysis of the streams in the simulated cluster suite Zinger et al. (2016) find that the penetration of the streams may change with streams either penetrating deeper or being pushed out over time. With the changes of stream penetration, new instances of collisions between streams and the surrounding gas can lead to the formation of shocks and CFs.

#### 4.2 Colliding Streams in CL107

In this section we present an additional example of a stream collision leading to the formation of shocks and CFs at the collision site.

The cluster CL107 has a virial mass of  $M_{\text{vir}} = 6.6 \times 10^{14} M_{\odot}$  and a virial radius of  $R_{\text{vir}} = 2.26 \text{ Mpc}$  at  $z = 0$  (see Table 1). Fig. 10 shows the gas and dark matter density of the cluster on a scale of several  $R_{\text{vir}}$ . The cluster is situated on a junction of 3 large scale filaments: one from the top right corner, one from the left and one from the bottom. Along the top right filament a merging cluster is poised to cross the virial radius in the near future. The accretion shock extends to  $\sim 2.8 R_{\text{vir}}$  (Zinger et al. in preparation).

A closer examination of these maps reveals that the gas from the prominent stream enters with the gas velocity of  $\sim 1000 \text{ km s}^{-1}$  from the top right, upon entering within the virial radius of the cluster, and bends its motion to the negative  $X$  direction, leading to the collision with another stream coming from the left in the inner region of the cluster.

In Fig. 11 we zoom in on the area of stream collision, and once again highlight important features with colored arrows. The shock front is roughly  $750 h^{-1} \text{ kpc}$  long, clearly visible in the temperature, pressure and density maps (Figs. 11d to 11f). Closer examination, especially in the pressure map (Fig. 11e), reveals that the shock front is comprised of two distinct shocks. The top one (red arrow) originates with the collision of the two gas streams, and the bottom one (green arrow) is due to a satellite galaxy.

The satellite galaxy, marked by the orange arrow, can be seen as a cold dense spot just behind the shock front, and is especially evident in the metallicity map (Fig. 11b), which also shows the dark matter density distribution. One can clearly see the highly enriched gas being stripped from the galaxy. The gas behind the top shock front (red arrow) can be seen to be nearly devoid of metals, and coupled with the absence of a dark matter sub-halo in that region, leading to the conclusion that this shock front did not originate from a satellite. Finding a satellite along the inflowing gas stream is expected since the streams mark the preferred direction of accretion into the cluster.

A CF is naturally found behind the two shock fronts and it too extends over quite a large distance (blue and purple arrows). When examining the density and metallicity of the ‘cold’ side of the CF, it seems that most of it may have originated in the merging satellite. It is thus unclear whether the CF formed naturally behind the collision shock, or that the CF is the interface between the hot post shock gas and the cooler, denser gas stripped from the satellite. It is of course possible that the two processes are involved.

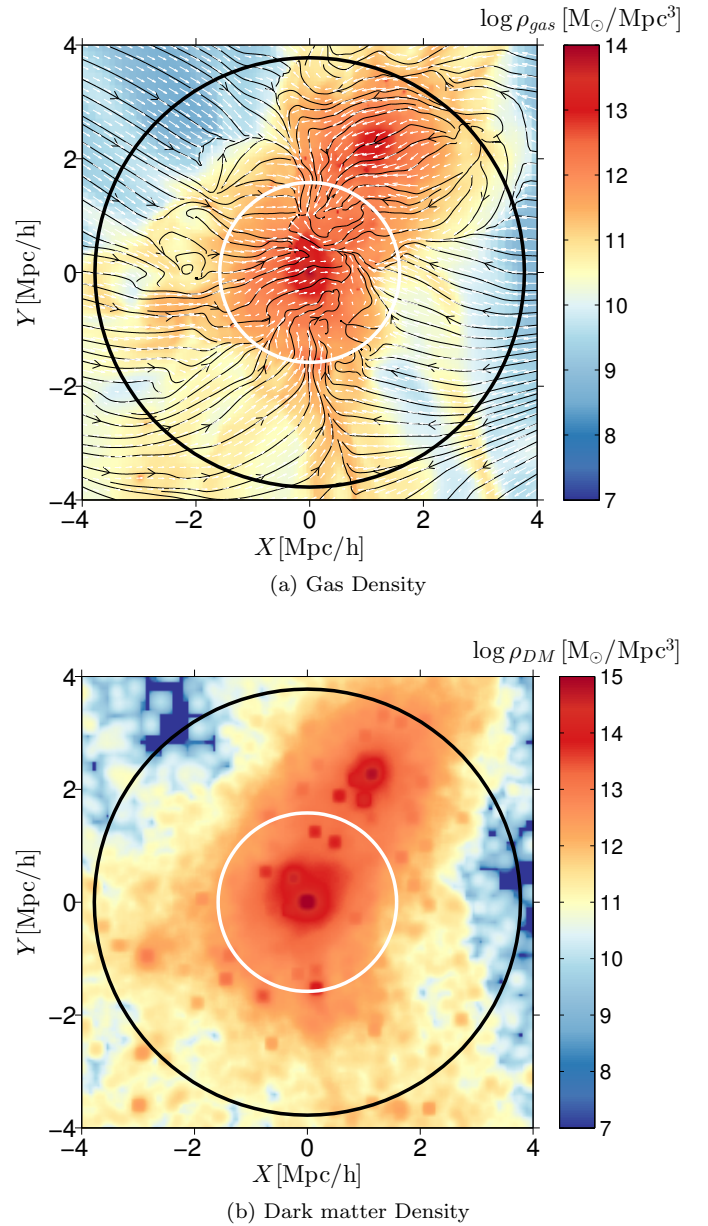


**Figure 10.** Gas (a) and dark matter density (b) of the cluster CL107 at  $z = 0$ . The maps and lines are created in the same way as those Fig. 3. An additional system, found in the top right quadrant, will soon cross the virial radius of the cluster.

As before we examine the profiles of various gas properties along two horizontal lines indicated in Fig. 11d, which are nearly perpendicular to the shock and CF. The top line located at  $X = 0.75 h^{-1} \text{ Mpc}$  goes through the upper, stream collision shock (Fig. 13), while the other line located at  $X = 0.5 h^{-1} \text{ Mpc}$  passes through the lower, merger induced shock (Fig. 12).

Along the bottom line of Fig. 11d, we find in Fig. 12 the merger induced shock at  $X = -0.33 h^{-1} \text{ Mpc}$  moving with the gas velocity of  $u_s \simeq -950 \text{ km s}^{-1}$  ( $\mathcal{M} \simeq 2.8$ ). The sign reversal of the parallel velocity component along the shock is a testament to the dramatic nature of head-on collision between the two streams. Behind the shock at  $X = -0.25 h^{-1} \text{ Mpc}$  a CF can be identified



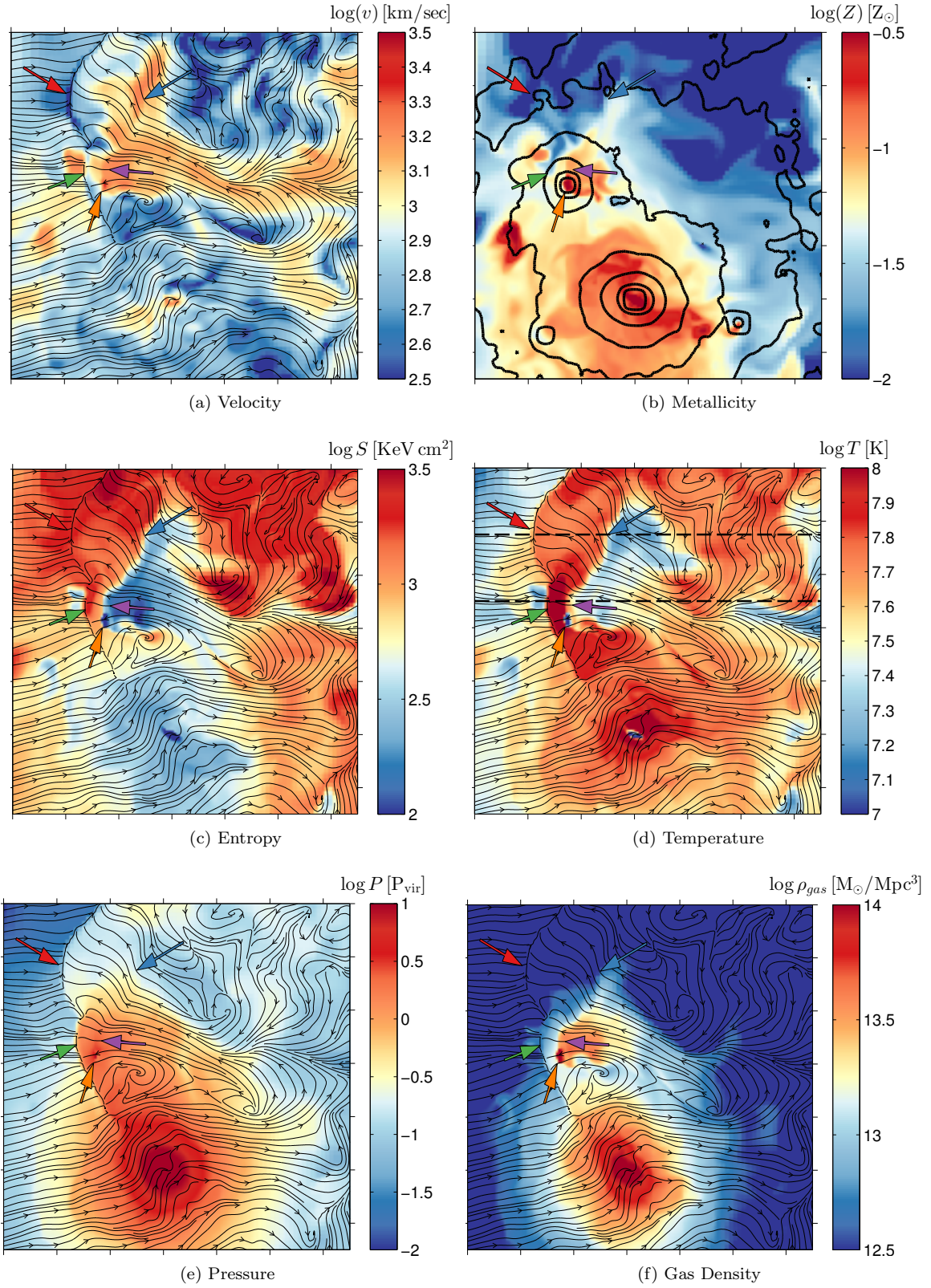
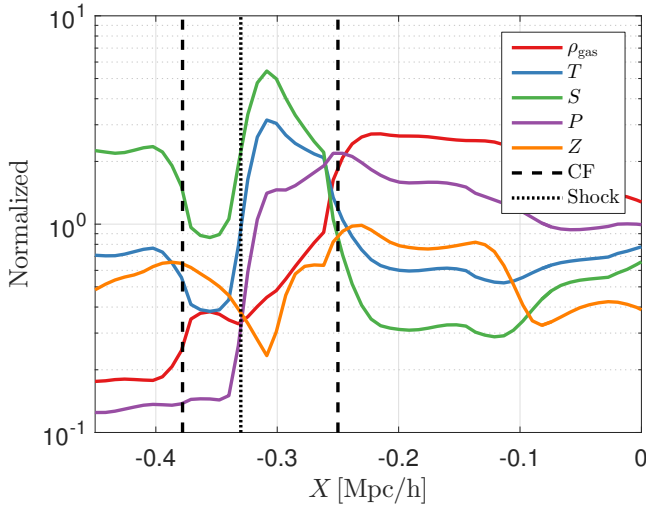
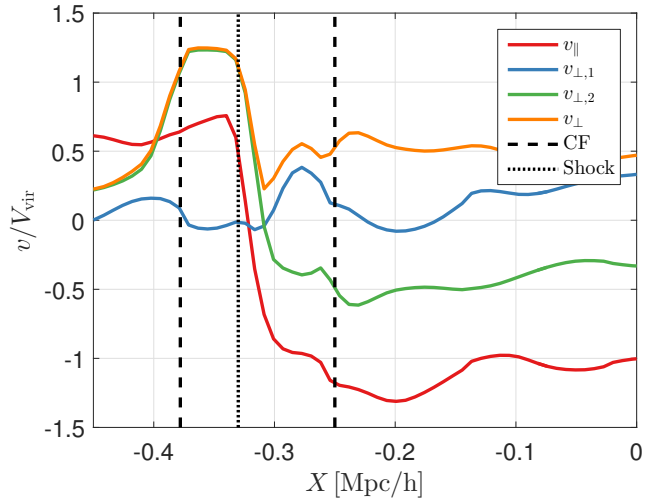


**Figure 11.** The collision zone between the two streams in CL107 at  $z=0$  is shown in detail in a box of side  $1.3h^{-1}$  Mpc centered around  $(0.05, 0.35)$  on the  $X-Y$  plane. The velocity (a) metallicity (b) entropy (c) temperature (d) pressure (e) and gas density (f) are all averaged over a slice of  $25h^{-1}$  kpc. Dark matter density contours (black) are shown in (b) (averaged over  $50h^{-1}$  kpc). Streamlines represent the velocity field. Areas of interest are marked by colored arrows as follows: the red & green arrows mark two shock fronts. The CFs are marked by blue & purple arrows. An orange arrow points to the satellite galaxy. The dashed horizontal lines shown in (d) mark the values used to follow the profiles of gas properties shown in Figs. 12 and 13.





(a) Thermodynamic Properties

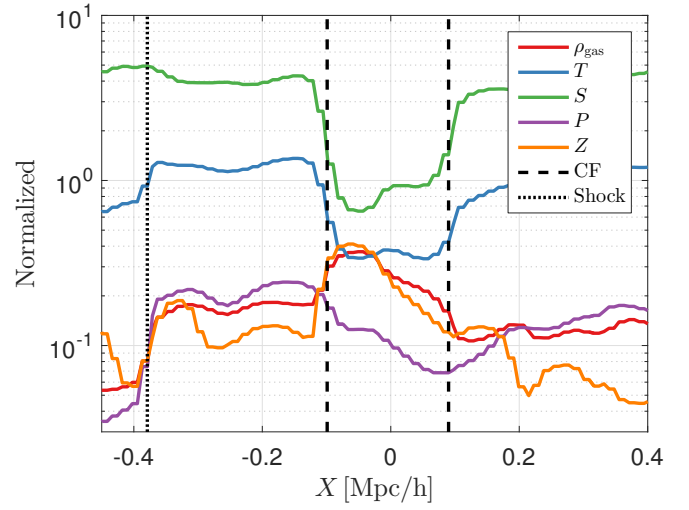


(b) Velocity Components

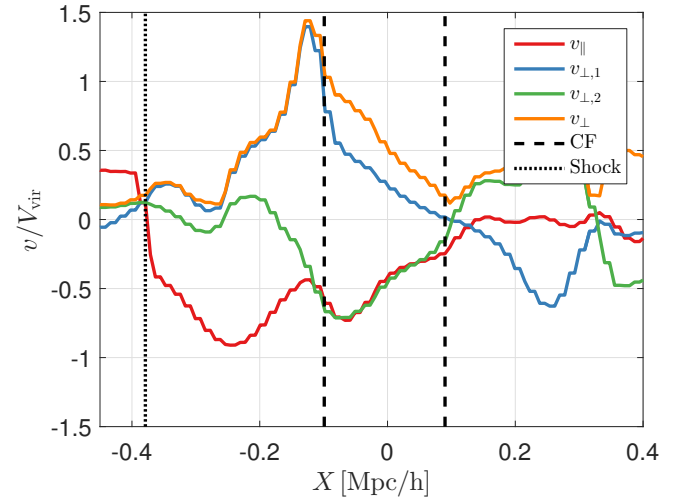
**Figure 12.** Profiles of the gas properties in CL107 at  $z = 0$  along a line in the  $X$  direction, perpendicular to the shock generated near the satellite and CF (green and purple arrows in Fig. 11) at  $Y = 0.5h^{-1}$  Mpc (see Fig. 11). Gas properties and line types are same as those in Fig. 7. Locations of shock fronts and CFs are also marked by black dotted and black dashed lines, respectively. The CF to the right of the shock is formed by stripping of gas the infalling satellite. The CF to the left of the shock is most likely a relic, which formed by the stream collision prior to the arrival of the satellite.

with density/temperature contrast of  $q \simeq 3.1$ . Another, smaller CF can be seen, just ahead of the shock wave at  $X = -0.38h^{-1}$  Mpc, with a density/temperature contrast of  $q \simeq 2$ . In both cases, the temperature and density contrasts are equal to within 5 per cent. While the first CF can be a result of the stream collision, the origin of the second one is not so clear, and may be a relic from an earlier event.

For the top line the shock is located at  $X = -0.38h^{-1}$  Mpc and moving with the gas velocity  $u_s \simeq -1300 \text{ km s}^{-1}$  ( $\mathcal{M} \simeq 1.9$ ). Two CFs can be seen at  $X = -0.1h^{-1}$  Mpc and  $X = 0.09h^{-1}$  Mpc. The contrasts for the density and temperature are not equal as in the other examples with a ratio of temperature to density contrasts,



(a) Thermodynamic Properties



(b) Velocity Components

**Figure 13.** Profiles of the gas properties (a) and velocity components (b) in CL107 along a line in the  $X$  direction, perpendicular to the shock and CF site formed by the stream collision (red and blue arrows in Fig. 11) at  $Y = 0.75h^{-1}$  Mpc (see Fig. 11). Gas properties and line types are the same as in Fig. 12. The sharp change in metallicity across the CF found on the left shows the enriched gas stripped from the satellites that are partially responsible for the formation of the CF.

which we designate as  $\eta$

$$\eta \equiv q_T q_\rho = \frac{T_1}{T_2} \frac{\rho_1}{\rho_2}, \quad (21)$$

and takes the values of  $\eta_1 = 1.8$  and  $\eta_2 = 0.8$  for the two CFs.

This shows that there is something different about the way these CF developed compared to the CF found in CL6. Unlike the other examples (Figs. 7 and 12), in which the metallicity profile showed little variation, the metallicity of the gas between the two CFs is markedly higher. In addition, the feature on the right while resembling a CF with a drop in temperature and a rise in density also has a drop in pressure, signifying that it may not be a CF but rather a region of

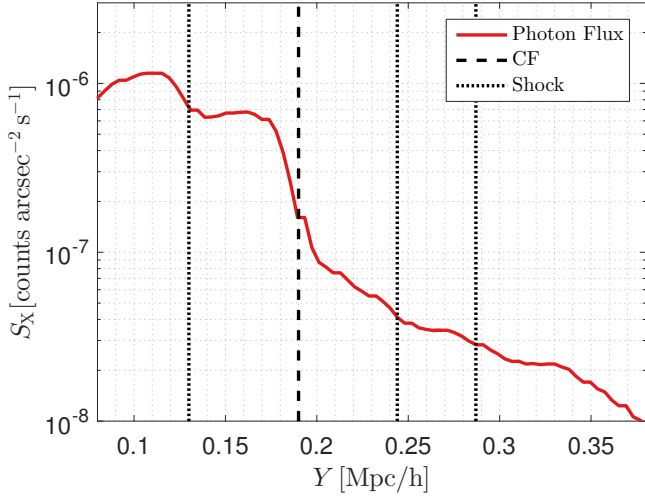


**Figure 14.** The X-ray surface brightness in the 0.5–2 keV range as estimated from the simulation data of CL6 along a line in the  $Y$  direction (and  $X = 0$ ), perpendicular to the shock and CF, at  $Z = -0.12h^{-1}$  Mpc (see Fig. 6d). Locations of shock fronts and CFs are also marked by black dotted and black dashed lines, respectively. The X-ray flux is summed over  $1 \text{ Mpc } h^{-1}$  along the  $X$  direction. The CF feature is clearly discernible and is potentially detectable with current observational instruments.

colder and denser gas pushing against a warmer and more dilute region.

The velocity along the line (red line in Fig. 13b) shows that the cooler gas is indeed travelling towards the left slightly faster than the gas beyond the interface. There is also a sharp change in the perpendicular velocity component across the CFs. This is in accordance with our earlier conclusion that the CF are due, at least in part, to the presence of gas which has been stripped from an infalling galaxy.

## 5 OBSERVATIONAL DETECTABILITY OF COLD FRONTS

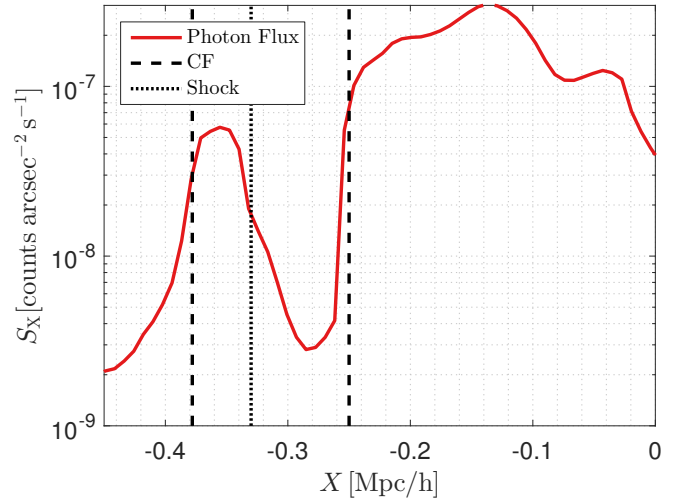
To predict the detectability of the CFs and shocks discussed above, we compute the X-ray surface brightness in the rest-frame energy band  $E = [0.5, 2.0]$  keV in the regions of interest of the clusters as would be observed by current instruments of the *Chandra* observatory.

Specifically, for each gas cell in the simulation, we compute the X-ray emissivity per unit volume within  $\epsilon(E)$  using the APEC plasma code (ver. 2.0.2 Smith et al. 2001; Foster et al. 2012):

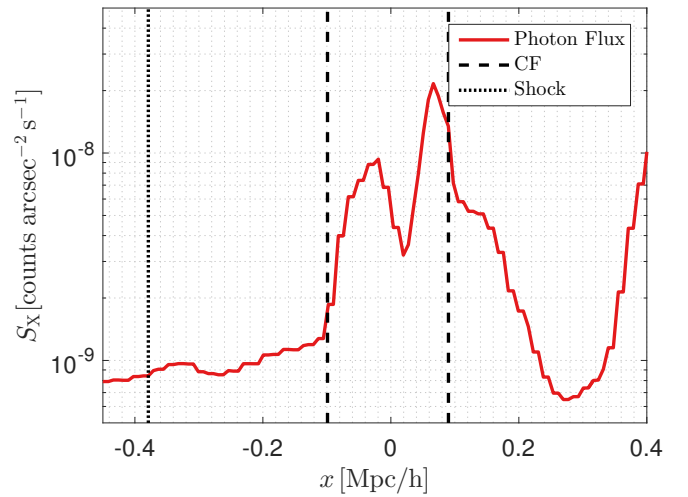
$$\epsilon(E) = n^2 \Lambda(E, T, Z, z), \quad (22)$$

where  $\Lambda(E, T, Z, z)$  is the specific cooling function from the APEC code,  $n$ ,  $T$ ,  $Z$  are the gas number density, temperature, and metallicity for each cell respectively, and  $z$  is the observed redshift of the cluster which we set to  $z = 0.06$ . For the energy band we are considering here, the emissivity is only weakly dependent on temperature and metallicity and is effectively a measure of the number density ( $\epsilon \propto n^2$ ).

The observed X-ray photon count per unit time  $f_x$  for each gas cell in the  $E = [0.5, 2.0]$  keV energy band is com-



(a) Bottom CF in CL107



(b) Bottom CF in CL107

**Figure 15.** The X-ray photon flux in the 0.5–2 keV range as estimated from the simulation data of CL107 along a two lines in the  $X$  direction at  $Y = 0.5h^{-1}$  Mpc (a) and  $Y = 0.75h^{-1}$  Mpc (b), perpendicular to the shock and CF site formed by the stream collision (see Fig. 11d). The X-ray flux is summed over  $2 \text{ Mpc } h^{-1}$  along the  $Z$  direction. The locations of shock fronts and CFs are marked by black dotted and black dashed lines, respectively. The low surface brightness in this regions most likely places these features beyond current observational capabilities.

puted as

$$f_x = \int_{0.5}^{2.0} \frac{\epsilon(E) l_c^3}{4\pi D_L(z)^2} \text{ARF}(E) dE, \quad (23)$$

where  $l_c$  is the cell-size,  $D_L(z)$  is the luminosity distance and  $\text{ARF}(E)$  is the effective area of the *Chandra* ACIS-I detector. We then sum up the contributions along the line of sight and find the surface brightness  $S_x$  by dividing by the angular area subtended by the simulation cell on the sky

$$S_x = \frac{f_x}{(l_c/D_A(z))^2}, \quad (24)$$

where  $D_A(z)$  is the angular diameter distance.

In Fig. 14 we show the X-ray surface brightness profile for the CF and shocks studied in CL6 along the same

line used for the profiles in Fig. 7 (see also Fig. 6d). In comparing the surface brightness profiles to the density profiles in Fig. 7a it is important to bear in mind that former are summed along the line of sight of the simulation data whereas the latter are *local* quantities.

The shock features are not very prominent but the drop in surface brightness associated with the CF is seen quite clearly. In terms of detectability, the surface brightness of the CF is of order  $10^{-7}$  counts arcsec $^{-2}$  sec $^{-1}$  which is within the observational capabilities of deep *Chandra* observations (e.g. Dasadia et al. 2016a,b). Thus, while the CF may be detected, the configuration of two opposite shocks with a CF in between, which marks the collision of an inflowing stream, will be difficult to identify.

In Figs. 15a and 15b we show the X-ray surface brightness profiles for the CF and shocks studied in CL107 for the bottom and top regions (respectively) along the same line used for the profiles in Figs. 12 and 13. The surface brightness for these features is lower by 1–2 orders of magnitude compared to the features in CL6, which most likely sets these features beyond current observational capabilities. The difference is not surprising since the features are found 2.5–3.5 times farther (in projected distance) from the centre of the cluster. For an isothermal-model ICM ( $\rho \propto r^{-2}$ ) the surface brightness is expected to drop as  $S_x \propto d^{-3}$ , where  $d$  is the projected distance from the cluster centre.

In this paper we have carried out an in-depth study of 2 examples of CFs linked to collisions of inflowing streams. It is important to note that these examples are by no means the only instance of CFs associated with stream collision in the simulation suite we have examined. A detailed study of all the clusters in our sample is beyond the scope of this work, but even a cursory search reveals that CFs are prevalent in all clusters, with many clusters hosting multiple CFs.

We wish to make a rough estimate as to the prevalence of CFs in the simulation suite and their detectability. To do so, we examined the  $z = 0$  snapshots of the 16-cluster simulation suite and visually identified CFs based on maps of the hydrodynamic and thermodynamic properties - temperature, density, pressure and entropy maps as well as metallicity and Mach number (e.g. Figs. 5 and 6). If a CF was found in close vicinity to an inflowing stream with no discernible satellite in the region and lacking a sharp metallicity gradient, it was marked as possibly linked to stream collisions. On average, we found approximately 6 CFs per cluster and of these,  $\sim 50$  per cent appear to be linked to inflowing streams.

Since the X-ray flux is a strong function of the gas density, we use the number density of the gas as a coarse estimate of detectability. In observational studies of shocks and CFs, a typical number density of features detectable with the *Chandra* observatory is  $\sim 10^{-3}$  cm $^{-3}$  (Markevitch & Vikhlinin 2007; Dasadia et al. 2016a,b). We use this value as a detectability limit and mark CFs with local densities above this value as possibly detectable. In total, roughly 15 per cent of all CFs are detectable with *Chandra* and of the sub-group of CFs linked to inflowing streams, roughly 13 per cent are detectable. These fractions will most likely be substantially larger for the next generation of X-ray missions, *Athena* (Nandra et al. 2013) and the *X-ray Surveyor* (Weisskopf et al. 2015).

## 6 SUMMARY AND DISCUSSION

In this paper we report a robust mechanism for generating shocks and CFs in the central regions of clusters via the inflowing gas streams, which are seen in simulations to be prevalent in many clusters. This mechanism should be particularly relevant in unrelaxed clusters (see e.g. Hallman et al. 2010) in which gas streams are seen to penetrate into the core (Zinger et al. 2016).

Inflowing gas streams account for most of the mass accretion into the systems and can travel at high velocities with  $\gtrsim 1000$  km s $^{-1}$ , carrying with them a significant amount of energy (Zinger et al. 2016). In clusters, they are heated to the virial temperature as they penetrate through the halo. When they reach the central regions they often collide either with other streams or with the existing ICM, leading to the formation of shocks and CFs.

We examined an idealized 1D scenario for a collision between two streams (or a single stream and the relaxed ambient gas) of constant density and pressure and found that as a result of the collision, two shocks are formed, propagating in opposite directions. Between the two shocks a contact discontinuity in density invariably forms, which travels at the velocity of the post-shock gas. The contact discontinuity is in pressure equilibrium, thus a jump in temperature is expected to be compensated by a drop in gas density, except in the exceptional case of completely identical streams in both density and pressure.

This simple, idealized picture is a far cry from the complex 3D structures and processes found in the ICM in observations and in simulations such as the ones analysed here. However, detailed examination of stream collisions in simulated clusters revealed configurations which resemble the idealized test-problem.

In the cluster CL6, at the site of the stream collision, two shocks moving in opposite directions were identified with a distinct CF found between them, whose density and temperature contrasts are (inversely) equal to within  $\lesssim 5$  per cent. The absence of any form of substructure and the dearth of metals in the gas at the CF location enables us to rule out satellites as a source of the CF. An additional shock, likely formed earlier, was found beyond the leading shock and analysis of the shock properties suggests that the shocks will merge and lead to the formation of another CF (Birnbom et al. 2010).

We investigated the CF formation in a fashion similar to observations, namely analysing a single snapshot to determine the link between the CFs and the streams that generated them. A future study, utilizing simulations with improved temporal resolution is planned in order to study the formation and evolution of CFs formed by stream collision over time.

The primary objective of this paper is to provide a proof of concept for the formation of shocks and CFs by the collisions of inflowing gas streams from the cosmic web. The particular clusters presented here were chosen since it demonstrated a clear and compelling example for the mechanism. The stream collision site was fortuitously situated in such a way as to allow easy visualization of the CF along the Cartesian projections of the simulation.

Examining the potential to detect such CFs in observations, we found that for prominent cases, such as the CF



found in CL6, observational detection is definitely within the current capabilities of deep *Chandra* observations, although identifying the full configuration of two oppositely oriented shocks with a CF in between may prove challenging.

It is important to note that the examples examined in this paper are by no means the only instance of CFs associated with stream collision in the simulation suite we have examined. A visual survey of the simulation suite found multiple CFs in all the simulated clusters with roughly half of the CFs showing a possible connection to the inflowing streams, and, in our rough estimation,  $\sim 15$  per cent of all CFs are potentially detectable.

Linking CFs to streams unequivocally is only possible with an in-depth analysis as presented in the paper, but we found that CFs results from the collision of inflowing streams in nearly all clusters we examined.

One such example is presented in §4.2, where we examine an additional cluster (CL107) in which colliding gas streams generate shocks and CFs. In this cluster, the shock front at the collision site is comprised of two distinct shocks, one originating from the stream collision and the other from the motion of a large satellite travelling with the stream. In the latter, the resulting CF contains a metallicity gradient across the CF, indicating that gas stripped from the satellite is partially responsible for the CF.

This additional example shows that it is at times difficult to disentangle the contribution of the gas flowing along the stream and contribution of the merging sub-structure to the formation of the shocks and CFs. Since the gas streams mark the preferred direction of accretion into the cluster, merging satellites are often found travelling along the inflowing streams.

In many of the other examples of CFs found at stream collision sites there were additional features, such as satellites, which made it difficult to link the CF to the stream unequivocally. To complement the findings in this paper, a study of the prevalence of CFs at stream collision sites and their properties is in order. In particular, it is important to ascertain how common this mechanism is compared to other processes which form CFs.

It may be argued that since both mergers and streams are simply aspects of the process of mass accretion, there is no point in differentiating between them as mechanisms of CF formation. However, merger events in the core are episodic by nature and their effect on the ICM only lasts for  $\sim 0.1$ – $1$  Gyr (Churazov et al. 2003; Tittley & Henriksen 2005; Ascasibar & Markevitch 2006) whereas the accretion through streams can be constant over much longer periods of time.

Beyond the simple considerations of detectability, the ability to observe CFs is dependent on their stability to various physical processes which can destroy them. Thermal conduction and particle diffusion, for example, can smear out the features of CFs on time-scales of  $\sim 10$  Myr (Markevitch & Vikhlinin 2007), which implies that in order for CFs to be observed as much as they are, they must either be formed frequently, or that other factors, such as magnetic fields (Carilli & Taylor 2002), are suppressing the thermal conduction. Magnetic fields can also suppress Kelvin-Helmholtz instabilities from breaking up CFs (Keshet et al. 2010; Roediger et al. 2013; ZuHone et al. 2011, 2015). Shocks

crossing the CF can also disrupt it via the Richtmyer-Meshkov instability (Brouillette 2002).

An important aspect of generating CF by stream collisions is that while individual CF may disappear, new ones will constantly form on time-scales of several Gyr as long as the streams persist. When comparing the cluster CL6 at two different epochs we found that the inflowing gas streams persisted over several Gyrs, but that the penetration depths and thus the shocks and CFs generated changed over time.

As a case in point, at the stream collision site at  $z = 0$  we found two shocks propagating upwards (red and green arrows in Fig. 6) which are expected to merge in  $\sim 350$  Myr. At the location where the shocks merge, a new CF will be formed (Birnboim et al. 2010). Another point to consider is that formation of CFs via stream collisions is a natural explanation for CFs found in clusters in which there is no evidence of merger events.

In absence of instruments that can directly observe the gas streams in clusters, identifying the shocks and CF formed at the collision site may afford an indirect way to identify the streams. Observation of a double shock configuration with a CF found in between, as presented above, would constitute a strong piece of evidence for the existence of gas streams in clusters, beyond the realm of cosmological simulations.

## ACKNOWLEDGEMENTS

We thank Neta Zinger for his assistance and advice. This work was partly supported by the grants ISF 124/12, I-CORE Program of the PBC/ISF 1829/12, BSF 2014-273, and NSF AST-1405962 and AST-1412768.

## REFERENCES

- Ascasibar Y., Markevitch M., 2006, *ApJ*, 650, 102
- Bialek J. J., Evrard A. E., Mohr J. J., 2002, *ApJ*, 578, L9
- Birnboim Y., Dekel A., 2003, *MNRAS*, 345, 349
- Birnboim Y., Keshet U., Hernquist L., 2010, *MNRAS*, 408, 199
- Birnboim Y., Padnos D., Zinger E., 2016, preprint
- Brouillette M., 2002, *Annual Review of Fluid Mechanics*, 34, 445
- Bryan G. L., Norman M. L., 1998, *ApJ*, 495, 80
- Carilli C. L., Taylor G. B., 2002, *ARA&A*, 40, 319
- Churazov E., Forman W., Jones C., Böhringer H., 2003, *ApJ*, 590, 225
- Dasadia S., et al., 2016a, *MNRAS*, 458, 681
- Dasadia S., et al., 2016b, *ApJ*, 820, L20
- Dekel A., Birnboim Y., 2006, *MNRAS*, 368, 2
- Dekel A., et al., 2009, *Nature*, 457, 451
- Ferland G. J., Korista K. T., Verner D. A., Ferguson J. W., Kingdon J. B., Verner E. M., 1998, *PASP*, 110, 761
- Foster A. R., Ji L., Smith R. K., Brickhouse N. S., 2012, *ApJ*, 756, 128
- Ghizzardi S., Rossetti M., Molendi S., 2010, *A&A*, 516, A32
- Haardt F., Madau P., 1996, *ApJ*, 461, 20
- Hallman E. J., Skillman S. W., Jeltrema T. E., Smith B. D., O’Shea B. W., Burns J. O., Norman M. L., 2010, *ApJ*, 725, 1053
- Kennicutt Jr. R. C., 1998, *ApJ*, 498, 541
- Kereš D., Katz N., Weinberg D. H., Davé R., 2005, *MNRAS*, 363, 2
- Kereš D., Katz N., Fardal M., Davé R., Weinberg D. H., 2009, *MNRAS*, 395, 160

- Keshet U., Markevitch M., Birnboim Y., Loeb A., 2010, *ApJ*, 719, L74
- Klypin A., Kravtsov A. V., Bullock J. S., Primack J. R., 2001, *ApJ*, 554, 903
- Kravtsov A. V., 1999, Ph.d. thesis, NEW MEXICO STATE UNIVERSITY, <http://adsabs.harvard.edu/abs/1999PhDT.....25K>
- Kravtsov A. V., Vikhlinin A., Nagai D., 2006, *ApJ*, 650, 128
- Landau L. D., Lifshitz E. M., 1959, Fluid Mechanics. Course of theoretical physics, Oxford: Pergamon Press
- Lau E. T., Nagai D., Avestruz C., Nelson K., Vikhlinin A., 2015, *ApJ*, 806, 68
- Markevitch M., Vikhlinin A., 2007, *Phys. Rep.*, 443, 1
- Markevitch M., et al., 2000, *ApJ*, 541, 542
- Nagai D., Kravtsov A. V., 2003, *ApJ*, 587, 514
- Nagai D., Vikhlinin A., Kravtsov A. V., 2007a, *ApJ*, 655, 98
- Nagai D., Kravtsov A. V., Vikhlinin A., 2007b, *ApJ*, 668, 1
- Nandra K., et al., 2013, preprint
- Owers M. S., Nulsen P. E. J., Couch W. J., Markevitch M., 2009, *ApJ*, 704, 1349
- Owers M. S., Nulsen P. E. J., Couch W. J., 2011, *ApJ*, 741, 122
- Reiss I., Keshet U., 2014, *Physical Review Letters*, 113, 071302
- Roediger E., Kraft R. P., Forman W. R., Nulsen P. E. J., Churazov E., 2013, *ApJ*, 764, 60
- Smith R. K., Brickhouse N. S., Liedahl D. A., Raymond J. C., 2001, *ApJ*, 556, L91
- Tittley E. R., Henriksen M., 2005, *ApJ*, 618, 227
- Weisskopf M. C., Gaskin J., Tananbaum H., Vikhlinin A., 2015, in EUV and X-ray Optics: Synergy between Laboratory and Space IV.
- White S. D. M., Rees M. J., 1978, *MNRAS*, 183, 341
- Zel'Dovich Y. B., Raizer Y. P., 2002, Physics of shock waves and high-temperature hydrodynamic phenomena. Dover Publications
- Zinger E., Dekel A., Birnboim Y., Kravtsov A., Nagai D., 2016, *MNRAS*, 461, 412
- ZuHone J. A., Markevitch M., Johnson R. E., 2010, *ApJ*, 717, 908
- ZuHone J. A., Markevitch M., Lee D., 2011, *ApJ*, 743, 16
- ZuHone J. A., Markevitch M., Ruszkowski M., Lee D., 2013, *ApJ*, 762, 69
- ZuHone J. A., Kunz M. W., Markevitch M., Stone J. M., Biffi V., 2015, *ApJ*, 798, 90